




Tuning the spectrum of near-field radiative heat transfer using Mie resonance based metamaterialsRamin Pouria  and Sheila Edalatpour *Department of Mechanical Engineering, and Frontier Institute for Research in Sensor Technologies,
University of Maine, Orono, Maine 04469, USA* (Received 6 July 2023; revised 26 October 2023; accepted 14 December 2023; published 8 January 2024)

Tuning the spectrum of near-field radiative heat transfer is crucial for many potential applications such as near-field thermophotovoltaic and thermophotonic power generation. Mie resonance based metamaterials are promising candidates for tuning the near-field spectra. In this manuscript, we utilize the Fourier modal method to perform nonapproximate simulations of near-field radiative heat flux between Mie resonance based metamaterials. By decomposing the electromagnetic response of the Mie resonators into contributions from various multipoles, we identify the origins of the peaks in the near-field spectra. We study the effect of the refractive index, extinction coefficient, shape, and interspacing of Mie resonators, as well as the separation distance of the metamaterials on the spectrum of near-field heat flux. Our study shows that as the refractive index of the metamaterial increases, the heat flux increases and the spectral locations of the Mie resonances redshift. As the extinction coefficient increases, the near-field heat flux increases and the damping of the Mie resonances eventually results in a broadband spectrum for the heat flux. Resonance splitting is observed when the distance between the Mie resonators approaches the nanometer scale. While the existing studies suggest that Mie resonance based metamaterials increase the near-field heat flux, the near-field heat transfer between these metamaterials is smaller than that between two thin films of the same material and thickness. However, Mie resonance based metamaterials are promising for tuning the spectrum of the near-field heat flux.

DOI: [10.1103/PhysRevB.109.045407](https://doi.org/10.1103/PhysRevB.109.045407)**I. INTRODUCTION**

Radiative heat transfer (RHT) exceeds the blackbody limit by orders of magnitude when the heat-exchanging media are separated by a gap smaller than the thermal wavelength [1]. The enhancement of RHT at subwavelength separation gaps, referred to as the near-field RHT (NFRHT), is due to the tunneling of exponentially decaying evanescent waves that are only substantial at subwavelength distances from the emitting surface [1,2]. Near-field radiative heat transfer has several promising applications such as nanogap thermophotovoltaic [3] and thermophotonic [4] power generation, thermal rectification [5,6], and near-field photonic cooling [7]. Tuning the spectrum of NFRHT is imperative for the development of these applications.

Metamaterials, which are materials engineered at the sub-wavelength scale [8], have been proposed for tuning the spectrum of NFRHT [9–15]. One class of the proposed metamaterials is the Mie resonance based metamaterials which are made of subwavelength particles of dielectric materials [16]. These subwavelength particles can thermally emit at Mie resonances causing sharp peaks in the spectrum of NFRHT. The Mie resonance based metamaterials are promising for NFRHT applications. They provide a mechanism for tuning the spectrum of NFRHT for the dielectric media that do not support surface phonon polaritons. Additionally, the spectrum of NFRHT for Mie resonance based metamaterials can be tuned to a great extent by changing the size, shape, and material properties of the resonators. Despite this potential, so far very few studies have focused on NFRHT in Mie resonance based metamaterials [16–20]. Using the effective medium theory (EMT), it was shown that the Mie resonance based metamaterials can have negative effective permeabil-

ity, in addition to negative effective permittivity, and thus they can emit the surface modes in both transverse electric (TE) and transverse magnetic (TM) polarizations [16–19]. The TE-polarized surface modes, which cannot be emitted from natural materials, introduce new peaks in the spectra of near-field heat flux and provide an additional channel for heat transfer [16–19]. The EMT, which treats the array of the subwavelength resonators as a semi-infinite planar medium with an effective permittivity and permeability, is known to be invalid for predicting both the spectrum and the magnitude of NFRHT [21]. Recently, NFRHT between two Mie resonance based metamaterials made of two-dimensional periodic arrays of tellurium cubes was studied using numerical simulations. It was shown that the Mie resonances cause peaks in the near-field spectra, and the locations of the peaks can be modulated by changing the size of the Mie resonators [20]. However, there is a knowledge gap about the origin of the peaks observed in the spectrum of NFRHT and how these peaks evolve as the material properties and the geometry of the array vary.

In this paper, we employ a nonapproximate numerical method, namely, the Fourier modal method (also known as the rigorous-coupled wave analysis) [22], to study the NFRHT between periodic arrays of Mie resonators for different material properties, separation gaps, and geometries. Using a multipole expansion of the scattering cross section of the individual Mie resonators [23], we identify the origin of various peaks observed in the spectrum of NFRHT. While previous studies indicate that the Mie resonance based metamaterials result in enhanced NFRHT [16–20], we show that indeed NFRHT between these metamaterials is always less than that for a thin film of the same material and thickness as the corresponding metamaterials. This study elucidates the physics

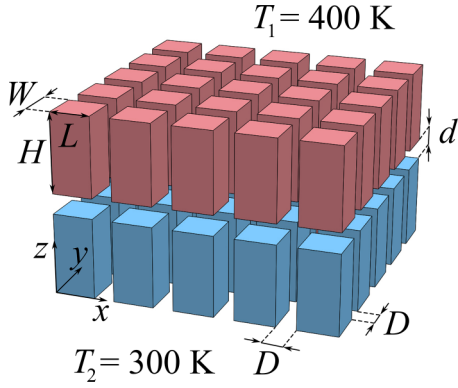


FIG. 1. A schematic of the system under study. Two Mie resonance based metamaterials made of two-dimensional periodic arrays of microcuboids are separated by a gap of size d . One of the metamaterials is at temperature $T_1 = 400$ K, while the other one is kept at temperature $T_2 = 300$ K. Near-field radiative heat transfer between the two metamaterials is desired.

underlying NFRHT between Mie resonance based metamaterials and can guide designing thermal emitters with the desired NFRHT spectrum.

This paper is organized as follows. The problem under study and the methods used for solving this problem are described in Sec. II. The results are described in Sec. III, and the concluding remarks are presented in Sec. IV.

II. DESCRIPTION OF THE PROBLEM AND METHODS

The problem under consideration is illustrated in Fig. 1. Two identical Mie resonance based metamaterials made of

two-dimensional periodic arrays of microcuboids are separated by a vacuum gap of size d . The cuboids have a side length L , a width W , a height H , and an interspacing D . The temperatures of the two metamaterials are fixed at $T_1 = 400$ K and $T_2 = 300$ K. The objective is to analyze the spectrum of NFRHT between the two metamaterials and study how the spectrum evolves as the material properties, the separation gap, and the geometry of the array change.

The near-field radiative heat flux between the metamaterials is found using the fluctuational electrodynamic theorem [1,2], and by applying the Fourier modal method, as implemented in the MESH software [22], for solving the stochastic Maxwell equations. A summary of the Fourier modal method used for numerical modeling of NFRHT is provided in the Appendix. To identify the peaks observed in the spectrum of the near-field heat flux, the scattering cross section of the microcuboids is decomposed into contributions from electric and magnetic dipoles and quadrupoles. The spectral locations of the Mie resonances in the scattering cross section are very close to those in the absorption cross section. As such, and due to the availability of the multipole expansion for the scattering cross section [23], we choose to decompose the scattering cross section into multipole contributions in this study. When an individual cuboid is illuminated with an incident electric field, $\mathbf{E}_{\text{inc}}(\mathbf{r}, \omega)$, a current is induced inside the cuboids. The induced current density is given by $\mathbf{J}_\omega(\mathbf{r}, \omega) = -i\omega\epsilon_0(\epsilon_r - 1)\mathbf{E}(\mathbf{r}, \omega)$, where \mathbf{r} , ω , $\mathbf{E}(\mathbf{r}, \omega)$, ϵ_0 , and ϵ_r are the position vector, angular frequency, electric field, permittivity of the free space, and dielectric function of the microcuboids, respectively. The moments of the electric and magnetic dipoles and quadrupoles are then found using the induced current density as [23]

$$p_\alpha = -\frac{1}{i\omega} \int \mathbf{J}_{\omega,\alpha} j_0(kr) d^3\mathbf{r} - \frac{k^2}{2i\omega} \int \frac{j_2(kr)}{(kr)^2} [3(\mathbf{r} \cdot \mathbf{J}_\omega) r_\alpha - r^2 J_{\omega,\alpha}] d^3\mathbf{r}, \quad (1a)$$

$$m_\alpha = \frac{3}{2} \int (\mathbf{r} \times \mathbf{J}_\omega)_\alpha \frac{j_1(kr)}{kr} d^3\mathbf{r}, \quad (1b)$$

$$Q_{\alpha\beta}^e = -\frac{3}{i\omega} \left\{ \int \frac{j_1(kr)}{kr} [3(r_\beta J_{\omega,\alpha} + r_\alpha J_{\omega,\beta}) - 2(\mathbf{r} \cdot \mathbf{J}_\omega) \delta_{\alpha\beta}] d^3\mathbf{r} + 2k^2 \int \frac{j_3(kr)}{(kr)^3} [5r_\alpha r_\beta (\mathbf{r} \cdot \mathbf{J}_\omega) - (r_\alpha J_{\omega,\beta} + r_\beta J_{\omega,\alpha}) r^2 - r^2 (\mathbf{r} \cdot \mathbf{J}_\omega) \delta_{\alpha\beta}] d^3\mathbf{r} \right\}, \quad (1c)$$

$$Q_{\alpha\beta}^m = 15 \int \frac{j_2(kr)}{(kr)^2} \{ r_\alpha (\mathbf{r} \times \mathbf{J}_\omega)_\beta + r_\beta (\mathbf{r} \times \mathbf{J}_\omega)_\alpha \} d^3\mathbf{r}, \quad (1d)$$

where p_α and m_α are the α ($\alpha = x, y, z$) component of the electric and magnetic dipole moments, respectively; $Q_{\alpha\beta}^e$ and $Q_{\alpha\beta}^m$ are the $\alpha\beta$ ($\beta = x, y, z$) element of the electric and magnetic quadrupole moment tensors, respectively; r is the magnitude of the position vector; i is the imaginary unit, k is the magnitude of the wave vector in the free space, and $j_n(kr)$ is the spherical Bessel function of the n th kind. The induced current density, \mathbf{J}_ω , required for finding the multipole moments using Eqs. 1(a)–1(d), is simulated using the COMSOL WAVE OPTICS MODULE. Once the electric and magnetic multipole moments are found, the contributions from each multipole to the total scattering cross section can be expressed

as [23]

$$\sigma_s^p = \frac{k^4}{6\pi\epsilon_0^2 |\mathbf{E}_{\text{inc}}|^2} \sum_\alpha |p_\alpha|^2, \quad (2a)$$

$$\sigma_s^m = \frac{k^4}{6\pi\epsilon_0^2 |\mathbf{E}_{\text{inc}}|^2} \sum_\alpha \left| \frac{m_\alpha}{c} \right|^2, \quad (2b)$$

$$\sigma_s^{Q^e} = \frac{k^6}{720\pi\epsilon_0^2 |\mathbf{E}_{\text{inc}}|^2} \sum_{\alpha\beta} |Q_{\alpha\beta}^e|^2, \quad (2c)$$

$$\sigma_s^{Q^m} = \frac{k^6}{720\pi\epsilon_0^2 c^2 |\mathbf{E}_{\text{inc}}|^2} \sum_{\alpha\beta} |Q_{\alpha\beta}^m|^2, \quad (2d)$$

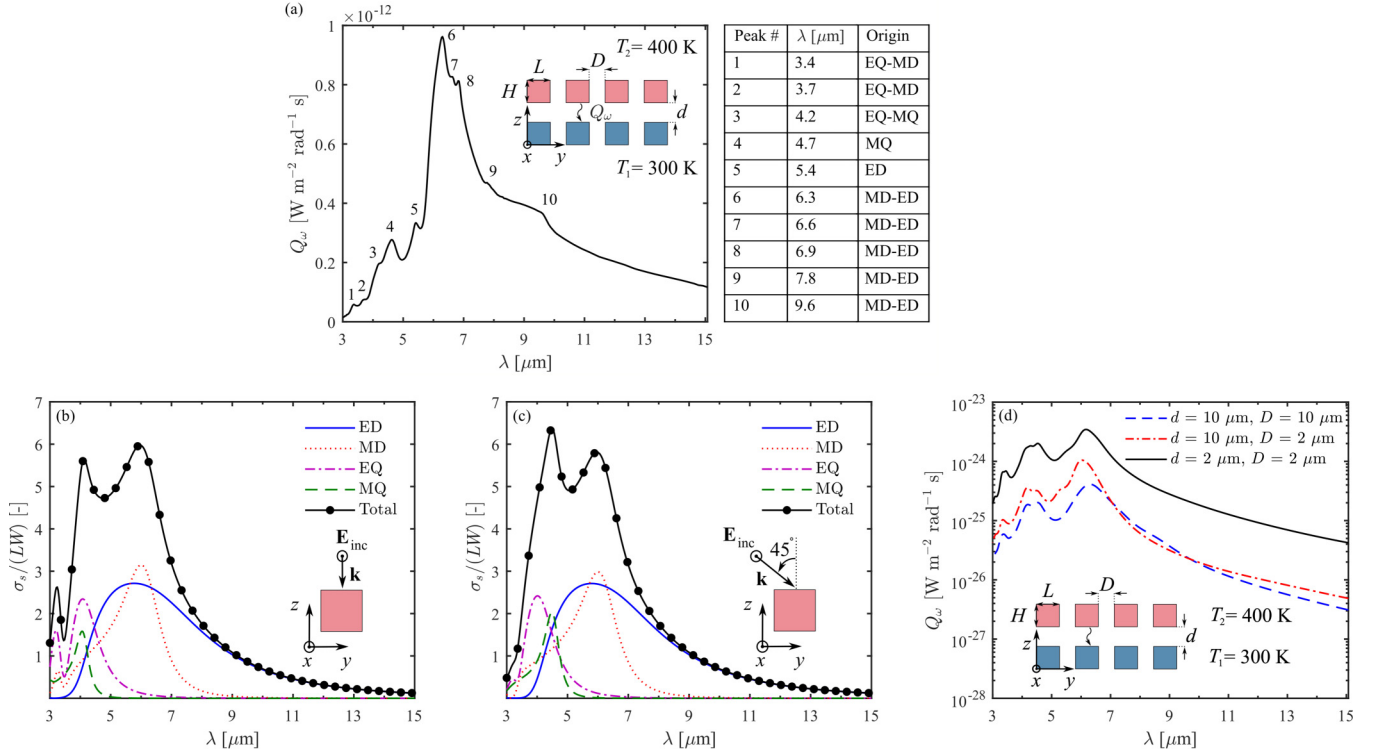


FIG. 2. (a) Near-field radiative heat flux between the two metamaterials shown in Fig. 1. The refractive index of the microcubes and the separation gap of the metamaterials are $\tilde{n} = 2.4 + 0.05i$ and $d = 1 \mu\text{m}$, respectively, while $L = H = W = D = 2 \mu\text{m}$. (b),(c) The scattering cross section of an individual microcube normalized by the geometrical cross section, when the microcube is illuminated by an incident plane wave. The incident electric field is polarized along the x axis, while it propagates along the z axis in panel (b) and at angle of 45° with respect to the z axis in panel (c). See the insets of panels (b),(c) for schematics. (d) The near-field heat flux between two two-dimensional finite arrays each made of 16 microcubes. $L = H = W = 2 \mu\text{m}$.

where c is the speed of light in the free space, and σ_s^p , σ_s^m , σ_s^{Qe} , and σ_s^{Qm} are the contributions of the electric dipole, magnetic dipole, electric quadrupole, and magnetic quadrupole to the scattering cross section of the Mie resonators, respectively. It should be noted that the contribution of the higher-order modes to the scattering cross section is negligible. This is confirmed by finding the total scattering cross section using the COMSOL WAVE OPTICS MODULE and comparing the result with the summation of σ_s^p , σ_s^m , σ_s^{Qe} , and σ_s^{Qm} found using Eqs. (2a)–(2d). Equations (2a)–(2d) are utilized to find the spectral locations of Mie resonances associated with each electric and magnetic multipole.

In addition to the scattering cross section of the Mie resonators, the distribution of the electric field within the resonators when the metamaterial is illuminated by an incident electric field is computed and used for identifying the Mie resonances in the near-field spectra. The electric-field distribution is modeled using the COMSOL WAVE OPTICS MODULE. The spectral NFRHT between nonperiodic arrays of Mie resonators is also found using the SCUFF-NEQ package of the SCUFF-EM electromagnetic solver [24] and is employed for interpreting the spectrum of near-field heat flux.

III. RESULTS AND DISCUSSION

Figure 2(a) shows the spectrum of NFRHT between two identical Mie resonance based metamaterials made of mi-

crocubes with side lengths $L = W = H = 2 \mu\text{m}$, and a cube's interspacing of $D = 2 \mu\text{m}$. Cubical resonators have been selected for this study since cubical microparticles can be fabricated using the standard optical lithography process. The complex refractive index and the separation gap of the two metamaterials are assumed as $\tilde{n} = 2.4 + 0.05i$ and $d = 1 \mu\text{m}$, respectively. The considered refractive index is close to the one for zinc selenide [24]. It should be noted that the considered refractive index may not follow the dispersion rule and the Kramers-Kronig relations. However, we proceed with this refractive index as the main objective of this study is to understand the effects of metamaterial parameters, such as the refractive index and extinction coefficient, on the spectrum of near-field heat flux. Ten peaks are observed in the near-field spectrum which are located at 3.4, 3.7, 4.2, 4.7, 5.4, 6.3, 6.6, 6.9, 7.8, and $9.6 \mu\text{m}$. To identify the origins of these peaks, the scattering cross section of an individual microcube when illuminated by an external electric field is computed and decomposed into contribution from the electric dipole (ED), magnetic dipole (MD), electric quadrupole (EQ), and magnetic quadrupole (MQ). The incident electric field is directed toward the x axis, and two incidence angles of 0° and 45° with respect to the z axis (i.e., normal and oblique incidence, respectively) are considered. Figures 2(b) and 2(c) show the decomposed scattering cross section of the microcubes normalized by the geometrical cross section (LW) for angles of incidence of 0° and 45° , respectively.

Figure 2(b) shows that the scattering cross section of the cubes for the normal incidence has three peaks which are located at 3.2, 4.1, and 6.0 μm . Considering the contributions from the ED, EQ, MD, and MQ modes to the scattering cross section as presented in Fig. 2(b), it is found that the peak at 3.2 μm is due to the EQ and MD modes (dominated by the contribution from the EQ), the peak at 4.1 μm is due to the EQ and MQ modes (with dominant contribution from the EQ mode), and the peak at 6.0 μm is due to contributions from the MD and ED modes (with dominant contribution from the MD mode). The spectral locations of the peaks in the spectrum of the scattering cross section for the oblique incidence shown in Fig. 2(c) are approximately the same as those for the normal incidence except for the peak associated with the EQ-MQ modes, which is slightly shifted from 4.1 to 4.5 μm . The microcubes in an array are close to each other, and thus the Mie modes of the neighboring microcubes can spatially overlap. This overlap causes resonant shift and/or splitting of the Mie resonances into a few peaks. For example, the radiative heat flux between two two-dimensional arrays made of 16 microcubes is simulated for separation gaps d and interspacing D of 10 and 2 μm using the SCUFF-NEQ package of the SCUFF-EM electromagnetic solver [25]. The results are shown in Fig. 2(d). The spectral locations of the peaks in the heat-flux spectrum for the case with $D = d = 10 \mu\text{m}$ are very similar to those of the scattering cross section of the individual microcubes. From left to right, the peaks in the heat-flux spectrum are due to the EQ-MD, EQ-MQ (observed for σ_s at normal incidence), EQ-MQ (observed for σ_s at oblique incidence), and MD-ED modes. When the interspacing decreases to $D = 2 \mu\text{m}$, the MD-ED mode splits into two peaks. With reducing the vacuum gap to $d = 2 \mu\text{m}$, the EQ-MD resonance also splits.

Considering the splitting and shift of the peaks caused by the spatial overlap of the Mie modes of the neighboring microcubes and using the decomposed scattering cross sections in Figs. 2(b) and 2(c), the peaks of NFRHT between the two metamaterials can be identified as follows. The peaks at 3.4 and 3.7 μm are both due to the EQ and MD modes (with dominant contribution from EQ), the peak at 4.2 μm is due to the EQ and MQ modes (with dominant contribution from MQ), the peak at 4.7 μm is due to the MQ modes supported at oblique incidence angles [see Fig. 2(c)], the peak at 5.4 μm is due to the ED mode, and the last five peaks at 6.3, 6.6, 6.9, 7.8, and 9.6 μm are all due to the ED and MD modes (with dominant contribution from the MD mode). The electric-field distributions within the cubes when the metamaterial is illuminated by an external electric field are also computed at the peaks' wavelengths. The electric fields are plotted in the y - z plane in the middle of the cubes (i.e., in the $x = \frac{L}{2}$ plane), when the metamaterial is excited by an electric field polarized in the x direction and incident at the normal direction [see Fig. 3(a)]. The magnitude of the incident electric field is assumed to be 1 V/m. The electric-field distributions at the peaks' wavelengths are provided in Fig. 3(b), and they are in agreement with the multipole decomposition analysis. It should be noted that as seen in Fig. 2(a), the NFRHT between the two Mie resonance based metamaterials is dominated by resonant thermal emission and absorption of the MD mode of the microcubes.

To study the effect of the refractive index on the spectrum of NFRHT between the Mie resonance based metamaterials, we increase the refractive index of the microcubes to $n = 3.5$, which is close to the refractive index of germanium telluride [26]. The other parameters of the array remain the same (i.e., $\kappa = 0.05$, $L = W = H = D = 2 \mu\text{m}$, and $d = 1 \mu\text{m}$). Figure 4(a) shows the spectral heat flux for this case. The normalized scattering cross sections for the normal and oblique incidence angles are also plotted in Figs. 4(b) and 4(c), respectively. Several new peaks appear in the heat-flux spectrum with increasing the refractive index. The appearance of the new peaks can be explained by comparing the scattering cross sections in Figs. 4(b) and 4(c) with those for a smaller refractive index of $n = 2.4$ presented in Figs. 3(b) and 3(c). It is seen that the spectral locations of the Mie modes are redshifted toward longer wavelengths as the refractive index increases. The magnetic modes, namely, the MD and MQ, experience the largest redshift. As n increases, the short-wavelength Mie modes redshift inside the considered spectral band, where they can be thermally excited. This redshift of the peaks results in the appearance of the new peaks in the heat flux spectra when n increases to 3.5.

In total, there are 16 peaks in the spectrum of near-field heat flux which can be identified using the decomposed scattering cross sections in Figs. 4(b) and 4(c) as well as the spatial distributions of the electric field inside the microcubes. The electric-field distribution at the peaks' wavelengths is shown in Fig. S1 of the Supplemental Material [27] for the incident electric field illustrated in Fig. 3(a). The wavelengths and the origins of the heat-flux peaks are listed in Fig. 4(a). Figure 4(a) also shows that the heat flux increases compared to the previous case with a smaller refractive index of $n = 2.4$. The greatest enhancement is seen in the wavelength range of 8–10 μm , where the MD modes are located. Thermal emission and absorption by the microcubes due to the MD modes are proportional to the imaginary part of the magnetic polarizability, $\text{Im}[\alpha^m]$ [28]. The imaginary part of the magnetic polarizability is proportional to $\text{Im}[\varepsilon]$, where ε is the dielectric function of the microcubes [28]. As n increases, $\text{Im}[\varepsilon]$ and $\text{Im}[\alpha^m]$ increase, which results in higher emission and absorption by the microcubes, thus increasing the heat flux. It should be noted that, similar to the case with a smaller refractive index of $n = 2.4$, the heat flux is dominated by the contribution from MD modes.

In Fig. 5, the refractive index of the microcubes is further increased to $n = 5.0$, which is approximately the same as the refractive index of tellurium [29]. The decomposed scattering cross sections at the normal and oblique incidence are provided in Figs. S2(a) and S2(b) of the Supplemental Material [27] for this case. With further increase of the refractive index, the Mie modes redshift and the heat flux increases further. The heat flux has 16 peaks associated with Mie resonances, which are identified and reported in Fig. 5. The heat flux is dominated by the contribution from six peaks located at 6.8, 7.2, 8.1, 8.9, 12.1, and 12.7 μm (peak numbers 8, 9, 10, 11, 15, and 16 in Fig. 5), which are due to the MD, EQ, MQ, ED, MD, and MD modes, respectively. Figure 5 shows that, similar to the case with $n = 3.4$, the MD modes significantly contribute to the heat flux. It is also seen that the contributions from the ED and EQ modes to the heat flux are greater for this

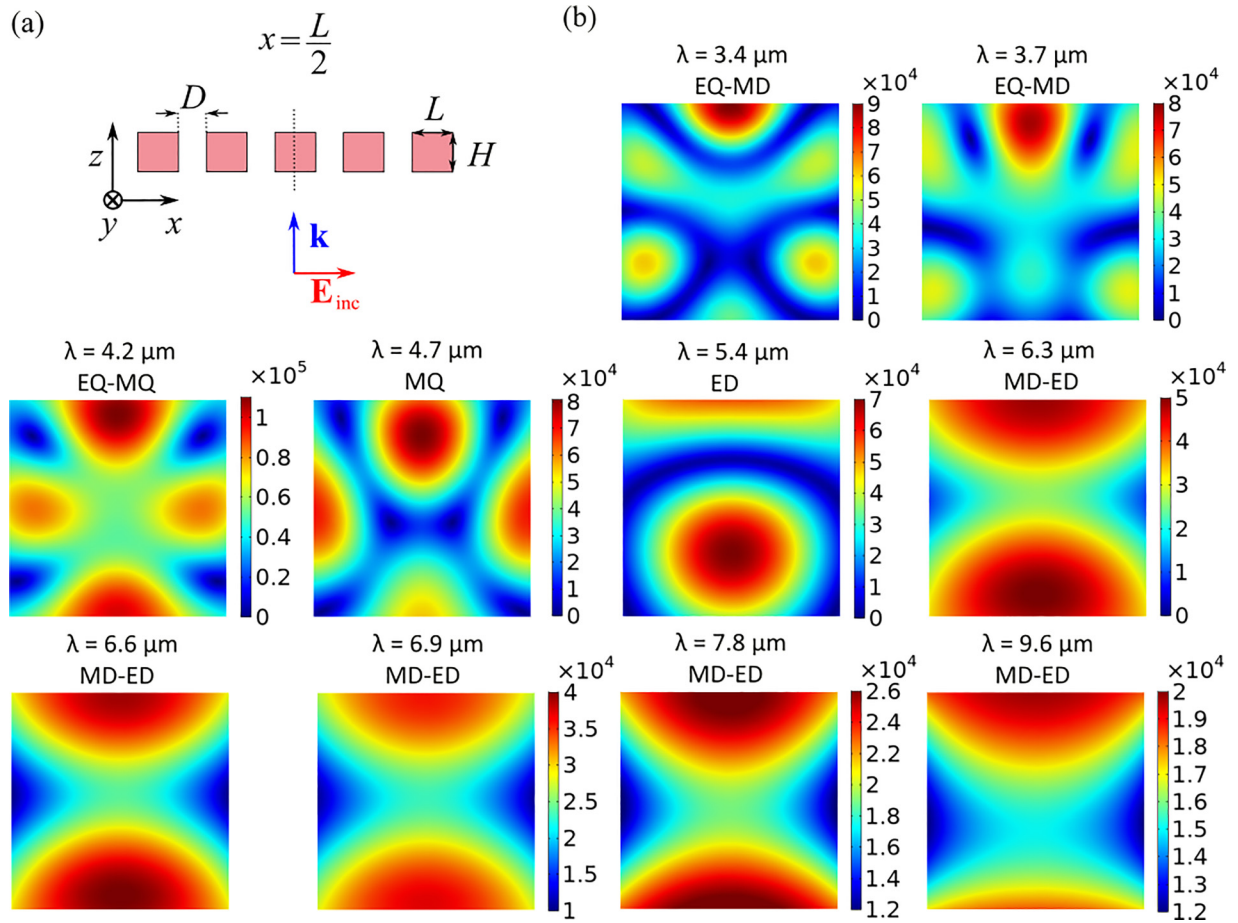


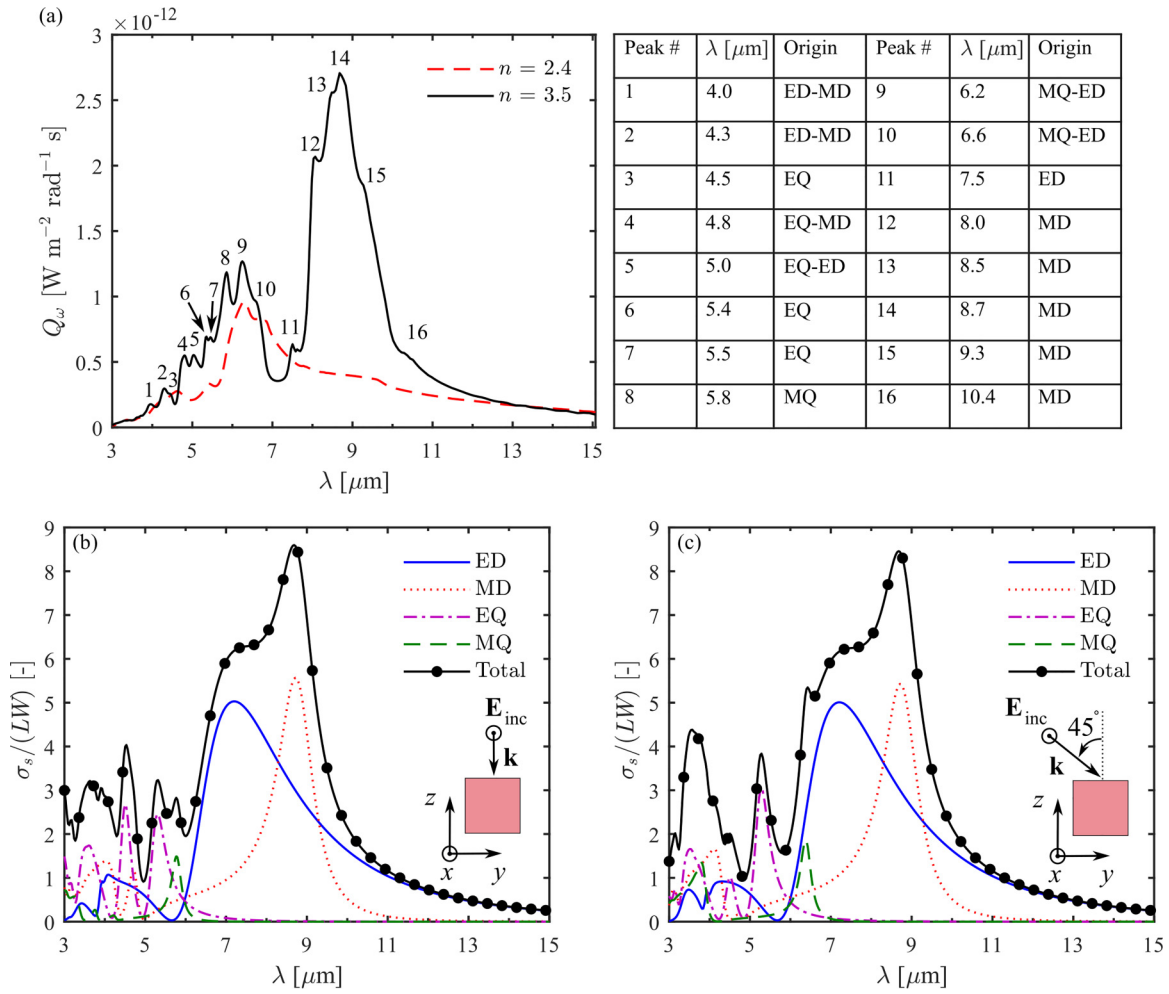
FIG. 3. (a) An electric field polarized along the x axis and propagating in the z direction is incident on the metamaterial. The magnitude of the incident field, \mathbf{E}_{inc} , is 1 V/m . (b) The spatial distribution of the induced electric field within the microcubes at the spectral locations of the NFRHT peaks. The electric field is plotted in the $x = \frac{L}{2}$ plane. The complex refractive index is $\tilde{n} = 2.4 + 0.05i$, while $L = W = H = D = 2 \mu\text{m}$ and $d = 1 \mu\text{m}$. The unit for the color bar is V/m .

case compared to the cases with smaller refractive indices of $n = 2.4$ and $n = 3.5$.

Next, we study the effect of extinction coefficient κ on the spectrum of heat flux. Figure 6(a) shows the NFRHT between two Mie resonance based metamaterials with $n = 5.0$ and three levels of extinction coefficient, namely, $\kappa = 0.05$, 0.1 , and 0.5 . With increasing κ from 0.05 to 0.1 , the spectral locations of the Mie resonances do not change. However, there is an enhancement of the heat flux at all wavelengths. As κ increases, $\text{Im}[\epsilon]$ and thus the thermally fluctuating current of the microcubes, given by the fluctuational electrodynamics [1,2], increase at all wavelengths. With increasing κ further to $\kappa = 0.5$, the broadband enhancement of the heat flux and the damping of the Mie resonances result in a broadband spectrum for the heat flux. Figure 6(a) shows that the extinction coefficient is a key factor in determining the shape of the heat-flux spectrum (spectrally selective or broadband).

The effect of microcube interspacing D on the NFRHT between the two Mie resonance based metamaterials is studied in Fig. 6(b). This figure shows the heat flux for three interspacing of $D = 2 \mu\text{m}$, $1 \mu\text{m}$, and 100 nm as well as for a thin film with the same material and thickness as the metamaterials. The refractive index is fixed at $\tilde{n} = 5.0 + 0.05i$, while the sizes of the microcubes and vacuum gap remain the same as in

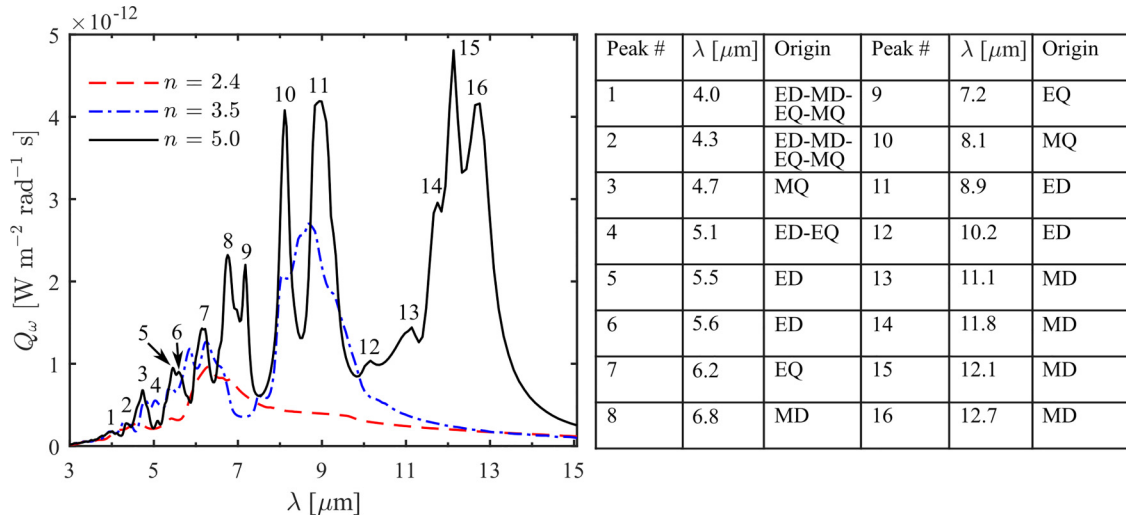
the previous cases (i.e., $L = W = H = 2 \mu\text{m}$ and $d = 1 \mu\text{m}$). As D decreases from 2 to $1 \mu\text{m}$, the heat flux increases in a broadband manner (i.e., at both resonance and nonresonance wavelengths). This enhancement is due to a larger volume of the Mie resonators per unit area of the metamaterials for the smaller interspacing of $D = 1 \mu\text{m}$. Reducing the interspacing to $D = 1 \mu\text{m}$ also results in the splitting of some of the Mie resonances such as the ED resonance at $10.2 \mu\text{m}$. The resonance splitting is due to the spatial overlap of the Mie modes of the neighboring microcubes as described before. When $D = 100 \text{ nm}$, the neighboring microcubes are placed at a near-field distance from each other. At near-field distances, the destructive interactions between the Mie modes result in damping of the heat-flux peaks except for the dominant dipole mode between $8 \mu\text{m}$ and $10 \mu\text{m}$, which is split into two peaks. However, the heat flux increases in a broadband manner when D decreases to 100 nm . As $D \rightarrow 0$, the spectrum of NFRHT approaches that for a thin film as shown in Fig. 7(b). It should be noted that the four peaks observed in the spectrum of heat flux for the thin films at 4.0 , 5.0 , 6.6 , and $9.8 \mu\text{m}$ are due to the fifth, fourth, third, and second Fabry-Perot interference resonances, respectively. The Fabry-Perot resonances are excited inside the thin films at wavelengths $\lambda = \frac{2nH}{N}$, where H ($=2 \mu\text{m}$) and N are the thickness of the film and the order of

FIG. 4. The same as Fig. 2 except for a complex refractive index of $\tilde{n} = 3.5 + 0.05i$.

the resonance, respectively. It should also be noted that, unlike in previous studies [16–20], the total heat flux for the Mie resonance based metamaterials is less than that for the thin films with the same refractive index and thickness. However, the Mie resonance based metamaterials provide more degrees

of freedom for designing the spectrum of NFRHT when compared to thin films.

To study the spectrum of NFRHT at smaller separation gaps, the spectral heat flux between two Mie resonance based metamaterials separated by a gap of size $d = 100$ nm is

FIG. 5. The same as Fig. 2(a) except for a complex refractive index of $\tilde{n} = 5.0 + 0.05i$.

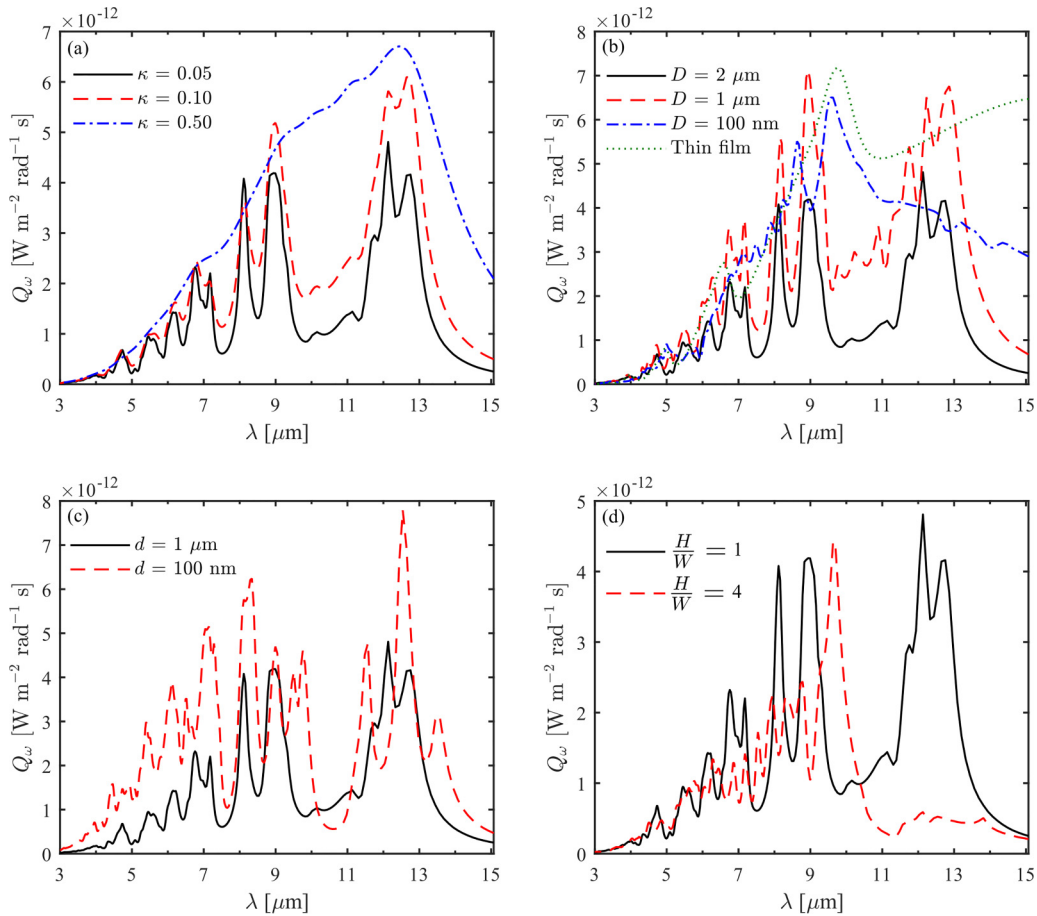


FIG. 6. The spectrum of near-field heat flux between the two Mie resonance based metamaterials schematically shown in Fig. 1. (a) The effect of the extinction coefficient κ on the heat flux. $L = W = H = D = 2 \mu\text{m}$, $n = 5.0$, and $d = 1 \mu\text{m}$. (b) The effect of cube interspacing D on the heat flux. $L = W = H = 2 \mu\text{m}$, $\tilde{n} = 5.0 + 0.05i$, and $d = 1 \mu\text{m}$. (c) The effect of the separation gap d on the heat flux. $L = W = H = D = 2 \mu\text{m}$ and $\tilde{n} = 5.0 + 0.05i$. (d) The effect of the geometry of the Mie resonators on the heat flux. $\tilde{n} = 5.0 + 0.05i$, $d = 1 \mu\text{m}$, and $L = W$. The array pitch is $4 \mu\text{m}$, and the volume of the Mie resonators is $8 \mu\text{m}^3$.

compared with the one for $d = 1 \mu\text{m}$ in Fig. 6(c). The complex refractive index of the microcubes is assumed to be $\tilde{n} = 5.0 + 0.05i$ for both cases. As expected, the heat flux increases as the gap size decreases. However, as the gap size decreases by one order of magnitude, the total (spectrally integrated) heat flux increases only by a factor of 2. This shows that the Mie resonance based metamaterials are suitable for intermediate near-field gaps (i.e., $d > 500 \text{ nm}$) which are experimentally more attainable. With decreasing the separation gap, the spectral locations of some of the Mie peaks such as the EQ slightly redshift. Additionally, the spatial overlap of the Mie modes results in splitting of the ED, MD, and MQ modes [see Fig. 6(c)].

Lastly, we show that the spectral locations and the relative intensity of the NFRHT peaks can be modulated to a great extent via varying the geometry of the Mie resonators. By changing the geometry of the resonators, it is possible to have several scattered peaks in the spectrum, or to spectrally overlap the Mie modes into a dominant peak. For example, Fig. 6(d) compares NFRHT for the microcube geometry studied so far ($L = W = H = 2 \mu\text{m}$) with that for a cuboidal geometry with edge lengths of $L = W = 1.26 \mu\text{m}$ and

$H = 5.04 \mu\text{m}$. The former has a height over width of $\frac{H}{W} = 1$, while this ratio for the latter is $\frac{H}{W} = 4$. The volume ($=8 \mu\text{m}^3$) and the array pitch ($=4 \mu\text{m}$), and thus the emitting volume per unit area of the metamaterials, are the same for both geometries. The refractive index is assumed to be $\tilde{n} = 5.0 + 0.05i$ for both cases. It is seen that for the case with $\frac{H}{W} = 1$, there are four dominant peaks at $8.1, 8.9, 12.1,$ and $12.7 \mu\text{m}$, which, as discussed before, are due to the MQ, ED, MD, and MD modes, respectively. When $\frac{H}{W} = 4$, the MD modes at 12.1 and $12.7 \mu\text{m}$ blueshift, while the MQ mode at $8.1 \mu\text{m}$ and the ED mode at $8.9 \mu\text{m}$ redshift. With the shift of the modes with changing the geometry, the MD, MQ, and ED modes spectrally overlap which results in a dominant peak in the spectrum of the near-field heat flux as seen in Fig. 6(d). In addition to the ratio $\frac{H}{W}$, the location and relative magnitude of the heat flux peaks can be tuned by varying the ratio $\frac{L}{W}$ of the cubes (for example, the spectral heat flux for two cases with $\frac{L}{W} = 1.0$ and $\frac{L}{W} = 1.5$ can be compared in Fig. S3 of the Supplemental Material [27]). It should be noted that even though a refractive index of $n = 5.0$ is assumed in Fig. 6, the effects of $\kappa, D, d,$ and $\frac{H}{W}$ on the spectrum of near-field heat flux for a smaller refractive index of $n = 2.4$ remain the

as [1]

$$e_{\parallel} = R_e L M_s^{-1} P \mathbf{J}, \quad (\text{A6a})$$

$$h_{\parallel}(z) = R_h L M_s^{-1} P \mathbf{J}. \quad (\text{A6b})$$

In Eqs. (A6a) and (A6b),

$$L = \begin{bmatrix} F_s(H-z') & \mathbf{O} \\ \mathbf{O} & F_s(z') \end{bmatrix},$$

$$P = \begin{pmatrix} \frac{1}{i\omega\epsilon_0} \frac{\partial}{\partial x} \eta_{zx} & \frac{1}{i\omega\epsilon_0} \frac{\partial}{\partial x} \eta_{zy} & \frac{1}{i\omega\epsilon_0} \frac{\partial}{\partial x} \eta_{zz} \\ \frac{1}{i\omega\epsilon_0} \frac{\partial}{\partial y} \eta_{zx} & \frac{1}{i\omega\epsilon_0} \frac{\partial}{\partial y} \eta_{zy} & \frac{1}{i\omega\epsilon_0} \frac{\partial}{\partial y} \eta_{zz} \\ 0 & 1 & 0 \\ -1 & 0 & 0 \end{pmatrix},$$

and

$$\begin{bmatrix} R_e \\ R_h \end{bmatrix} = M_r \begin{bmatrix} F_r(z_0) D_1 \\ F_r(H-z_0) D_2 \end{bmatrix} K_1^{-1} [\mathbf{I} \quad K_2],$$

where $K_1 = \mathbf{I} - F_s S_{12}(s^-, 0) F_s S_{21}(s^+, 4)$ and $K_2 = -F_s S_{12}(s^-, 0)$, and $D_1 = [\mathbf{I} - S_{12}(s^+, r) S_{21}(r, N)]^{-1} S_{11}(s^+, r)$ and $D_2 = S_{21}(r, N) D_1$ [22]. In these equations, the subscripts s and r refer to the source and receiver layers, respectively; $S_{ij}(m, n)$ is the element ij of the scattering matrix between layers m and n ; \mathbf{I} is the unit matrix; z' is the z component of the location of the source; z_0 is the location at which the electromagnetic field is evaluated; η is the inverse of the dielectric tensor ϵ ; and s^+ and s^- are two artificial layers with

a thickness of 0 defined at the top and bottom surfaces of emitting layer s , respectively. The s^+ and s^- layers have the same dielectric function as layer s .

Comparing Eqs. (A6) with (A2), the electric and magnetic Green's functions are found as

$$\mathbf{G}_e = R_e L M_s^{-1} P, \quad (\text{A7a})$$

$$\mathbf{G}_h = R_h L M_s^{-1} P. \quad (\text{A7b})$$

Substituting Eqs. (A7a) and (A7b) into Eq. (A4) and evaluating the integral, the spectral heat flux between the two metamaterials is found as [22]

$$Q_{\omega} = \frac{2\epsilon_0\omega}{\pi} [\Theta(\omega, T_3) - \Theta(\omega, T_1)] \text{Re} \\ \times \{ \text{Tr}[\Pi^{\dagger} R_e \{ [M_s^{-1} P \Gamma P^{\dagger} (M_s^{-1})^{\dagger}] \circ Y \} R_h^{\dagger}] \}, \quad (\text{A8})$$

where \circ indicates the Hadamard product and matrix $Y = \begin{bmatrix} y_1 & y_2 \\ y_2 & y_1 \end{bmatrix}$ is defined as [22]

$$Y_{1,(mn)} = \frac{1 - e^{-i(q_m - q_n^*)H}}{i(q_m - q_n^*)}, \quad (\text{A9a})$$

$$Y_{2,(mn)} = \frac{e^{iq_n^*H} - e^{-iq_mH}}{i(q_m - q_n^*)}. \quad (\text{A9b})$$

In Eq. (A9), q_m and q_n are the m th and n th eigenvalues of the electromagnetic field, respectively.

-
- [1] Z. M. Zhang, *Nano/Microscale Heat Transfer*, 2nd ed. (Springer, Cham, Switzerland, 2020).
- [2] K. Joulain, J. P. Mulet, F. Marquier, R. Carminati, and J. J. Greffet, Surface electromagnetic waves thermally excited: Radiative heat transfer, coherence properties and Casimir forces revisited in the near-field, *Surf. Sci. Rep.* **57**, 59 (2005).
- [3] C. Lucchesi, D. Cakiroglu, J. P. Perez, T. Taliercio, E. Tournié, P. O. Chapuis, and R. Vaillon, Near-field thermophotovoltaic conversion with high electrical power density and cell efficiency above 14%, *Nano Lett.* **21**, 4524 (2021).
- [4] J. Legendre and P. O. Chapuis, Overcoming non-radiative losses with AlGaAs PIN junctions for near-field thermophotonic energy harvesting, *Appl. Phys. Lett.* **121**, 193902 (2022).
- [5] C. R. Otey, W. T. Lau, and S. Fan, Thermal rectification through vacuum, *Phys. Rev. Lett.* **104**, 154301 (2010).
- [6] S. Basu and M. Francoeur, Near-field radiative transfer based thermal rectification using doped silicon, *Appl. Phys. Lett.* **98**, 113106 (2011).
- [7] L. Zhu, A. Fiorino, D. Thompson, R. Mittapally, E. Meyhofer, and P. Reddy, Near-field photonic cooling through control of the chemical potential of photons, *Nature (London)* **566**, 239 (2019).
- [8] W. Cai and V. M. Shalaev, *Optical Metamaterials*, 1st ed. (Springer, New York, 2010).
- [9] M. S. Mirmoosa, M. Omelyanovich, and C. R. Simovski, Microgap thermophotovoltaic systems with low emission temperature and high electric output, *J. Opt.* **18**, 115104 (2016).
- [10] K. Li, S. Wu, S. Cao, Q. Cai, Q. Ye, X. Liu, and X. Wu, Transient performance of a nanowire-based near-field thermophotovoltaic system, *Appl. Therm. Eng.* **192**, 116918 (2021).
- [11] Y. Taniguchi, K. Isobe, and K. Hanamura, Enhancement of spectrally controlled near-field radiation transfer by magnetic polariton generated by metal-insulator-metal structures, *Appl. Therm. Eng.* **183**, 116041 (2021).
- [12] J. Y. Chang, Y. Yang, and L. Wang, Tungsten nanowire based hyperbolic metamaterial emitters for near-field thermophotovoltaic applications, *Int. J. Heat Mass Transfer* **87**, 237 (2015).
- [13] H. Yu, Y. Duan, and Z. Yang, Selectively enhanced near-field radiative transfer between plasmonic emitter and GaSb with nanohole and nanowire periodic arrays for thermophotovoltaics, *Int. J. Heat Mass Transfer* **123**, 67 (2018).
- [14] J. I. Watjen, X. L. Liu, B. Zhao, and Z. M. Zhang, A computational simulation of using tungsten gratings in near-field thermophotovoltaic devices, *J. Heat Transfer* **139**, 052704 (2017).
- [15] V. Fernández-Hurtado, F. J. García-Vidal, S. Fan, and J. C. Cuevas, Enhancing near-field radiative heat transfer with Si-based metasurfaces, *Phys. Rev. Lett.* **118**, 203901 (2017).
- [16] M. Francoeur, S. Basu, and S. J. Petersen, Electric and magnetic surface polariton mediated near-field radiative heat transfer between metamaterials made of silicon carbide particles, *Opt. Express* **19**, 18774 (2011).
- [17] S. J. Petersen, S. Basu, B. Raeymaekers, and M. Francoeur, Tuning near-field thermal radiative properties by quantifying sensitivity of Mie resonance-based metamaterial design parameters, *J. Quant. Spectrosc. Radiat. Transfer* **129**, 277 (2013).

- [18] S. J. Petersen, S. Basu, and M. Francoeur, Near-field thermal emission from metamaterials, *Photonics Nanostruct. Fundam. Appl.* **11**, 167 (2013).
- [19] A. Ghanekar, Y. Tian, S. Zhang, Y. Cui, and Y. Zheng, Mie-metamaterials-based thermal emitter for near-field thermophotovoltaic systems, *Materials* **10**, 885 (2017).
- [20] Y. Hu, H. Li, Y. Zhang, Y. Zhu, and Y. Yang, Enhanced near-field radiation in both TE and TM waves through excitation of Mie resonance, *Phys. Rev. B* **102**, 125434 (2020).
- [21] S. Zare, R. Pouria, and S. Edalatpour, Validity of the effective medium theory for modeling near-field thermal emission by nanowire arrays, *J. Quant. Spectrosc. Radiat. Transfer* **261**, 107482 (2021).
- [22] K. Chen, B. Zhao, and S. Fan, MESH: A free electromagnetic solver for far-field and near-field radiative heat transfer for layered periodic structures, *Comput. Phys. Commun.* **231**, 163 (2018).
- [23] R. Alaei, C. Rockstuhl, and I. Fernandez-Corbaton, An electromagnetic multipole expansion beyond the long-wavelength approximation, *Opt. Commun.* **407**, 17 (2018).
- [24] D. Li, M. Jiang, H. Qi, Q. Wang, and C. Liu, Optical constants of zinc selenide at 373 and 423 K in the wavelength range of 2–15 μm , *J. Appl. Spectrosc.* **83**, 512 (2016).
- [25] M. T. H. Reid and S. G. Johnson, Modeling non-equilibrium electromagnetic fluctuations with SCUFF-NEQ, <http://homerreid.github.io/scuff-em-documentation/applications/scuff-neq/scuff-neq>.
- [26] E. N. Kotlikov, V. A. Ivanov, V. G. Pogareva, and E. V. Khonineva, Study of optical constants of PbTe and GeTe films, *Opt. Spectrosc.* **88**, 718 (2000).
- [27] See Supplemental Material at <http://link.aps.org/supplemental/10.1103/PhysRevB.109.045407> for the spatial distribution of the induced electric field within the microcubes for a refractive index of 3.5, the multipole expansion of the scattering cross section for a refractive index of 5.0, the effect of cubes' length to width ratio on the spectrum of near-field heat flux, and the effect of metamaterials' parameters on the spectrum of near-field heat flux for a refractive index of 2.4.
- [28] P. O. Chapuis, M. Laroche, S. Volz, and J. J. Greffet, Radiative heat transfer between metallic nanoparticles, *Appl. Phys. Lett.* **92**, 201906 (2008).
- [29] J. C. Ginn, I. Brener, D. W. Peters, J. R. Wendt, J. O. Stevens, P. F. Hines, L. I. Basilio, L. K. Warne, J. F. Ihlefeld, P. G. Clem *et al.*, Realizing optical magnetism from dielectric metamaterials, *Phys. Rev. Lett.* **108**, 097402 (2012).